2006

Fluid-structure analysis of microparticle transport in deformable pulmonary alveoli

Hannah L. Dailey
Lehigh University

Dailey, Hannah L.

Fluid-Structure Analysis of Microparticle Transport in Deformable Pulmonary Alveoli

January 2006

Fluid-Structure Analysis of Microparticle Transport in Deformable Pulmonary Alveoli

by

Hannah L. Dailey

A Thesis

Presented to the Graduate and Research Committee

of Lehigh University

in Candidacy for the Degree of

Master of Science

in

Mechanical Engineering and Mechanics

Lehigh University

January, 2006

CERTIFICATE OF APPROVAL

This thesis is accepted and approved in partial fulfillment of the requirements for the Master of Science.

12/1/05

Thesis Advisor Date

12/6/05

Department Chairman Date

TABLE OF CONTENTS

LIST OF TABLES AND FIGURES

ABSTRACT

Micron-sized particles inhaled into the respiratory system can traverse the airway tree and deposit on the walls of the pulmonary alveoli. The fate of these particles can be measured by their propagation depth, wall deposition rate, and time to impaction. These three quantities will depend on various physical parameters including particle size, breathing frequency, and viscoelastic tissue properties. This study develops a fluid-structure computational model of alveolar dynamics to quantify how these parameters influence particle transport in the deep lung and to identify the relative importance of convection and diffusion at the alveolar scale. The computational model simulates negative pressure breathing conditions in which applied tissue forces deform the lung parenchyma and produce oscillatory flow within the alveoli. The transient flow fields from the fluid-structure models are used to calculate the trajectories of micron-sized particles (i.e. 0.1 to 5 μm). Particle motion is governed by the Langevin equation, which contains a stochastic Brownian force term. The results indicate that Brownian diffusion dominates the transport and deposition of particles with a diameter less than 1 μm. Convection forces become increasingly dominant for larger particles and faster breathing rates and stiffer, more viscous tissues generate less wall motion and lower convection forces. Gravitational sedimentation is also a significant deposition mechanism for larger particles. This information may be useful in designing more effective inhaled pharmaceuticals or drug delivery strategies and in treating patients with compromised lung function due to disease or occupational injury.

KEYWORDS

Brownian diffusion, deep lung deformation, fluid-structure interactions, alveolar mechanics, tissue mechanics, biofluid dynamics

I. INTRODUCTION

The subject of particle transport in the human lungs has received much attention due to the wide range of pathogens, pharmaceuticals, and occupational hazards a person may inhale. Although several previous investigations have focused on transport phenomena in the conducting airways [1-3], micron-sized particles may traverse the larger airways and become deposited in the alveolar region of the lungs. Common pathogenic examples include the Respiratory Syncytial Virus (RSV) and Human Parainfluenza Viruses (HPIVs). RSV and HPIV are the two leading causes of lower respiratory tract disease in young children [4, 5]. The highly-vascularized alveolar region is also an important target location for the deposition of various pharmaceutical agents including α1-antitrypsin for emphysema [6] and aerosolized insulin or immunoglobulin [7]. In the workplace, inhalation of fine carbon and silica particles can lead to Coal Workers' Pneumoconiosis (black lung disease) and Silicosis [8, 9]. These examples indicate that a better understanding of particle transport dynamics in the deep lungs has broad clinical significance.

The complex anatomy and biophysics of the alveolar system presents several modeling challenges including alveolar interconnectivity, tissue-driven wall motion, and Brownian-diffusive particle dynamics. The lung parenchyma is sponge-like network of interconnected alveolated ducts and sacs. Neighboring alveoli share thin, flat walls and a common flow source. In addition, the alveolar honeycomb is not a static structure; it stretches and recoils with each breath. Fine particulates that migrate to the alveolar region are subject to convection, gravity, and random Brownian diffusion. However, Brownian diffusion operates on a much shorter time scale than the tidal breathing cycle, so including its effect can be a computationally expensive procedure. These potential modeling difficulties suggest that a tractable model of this system requires several simplifying assumptions.

Several recent studies of airflow and particle dynamics in the alveolar region of the lung approximate the alveoli as rigid structures. Tsuda [10] and colleagues used a series of

axisymmetric tori to simulate airflow and diffusive particle transport through an alveolated duct. They reported that particle deposition percentages in alveolated ducts were lower than the percentages observed in smooth ducts and that deposition rates were higher near the alveolar entrance ring. Darquenne [11] used computational techniques to track particle motion in a static six-generation tree of flat-walled alveolated ducts. Although this study neglected Brownian diffusion, Darquenne's models did document significant local particle deposition inhomogeneity after forced inspiration and expiration. While these models provide interesting insights, they ignore the alveolar wall motions that generate airflow and drive particle transport in the lungs.

Some investigators have addressed this problem by prescribing pre-defined alveolar wall motions. For example, Henry [12] and colleagues applied sinusoidal oscillations to semi-circular alveolar tori in a duct. Although they neglected Brownian diffusion, they concluded that alveolar wall motion induces chaotic mixing, which may be a mechanism of aerosol deposition. Haber and colleagues [13] studied gravitational deposition of aerosols in a rhythmically expanding and contracting 3-D alveolus and determined that wall motion is a critical factor in particle deposition. These studies underscore the need to consider domain deformation when simulating the kinetics and fluid mechanics of aerosol transport in the deep lung.

The current study presents a model for the transport of micron-sized particles in the alveolus that addresses the challenges discussed above, i.e. alveolar interconnectivity, tissue-driven wall motion, and Brownian-diffusive particle dynamics. The models represent the alveolar sac as a cluster of flat-walled subunits sharing structural and fluid dynamic connectivity with their neighbors. These structures mimic the hexagonal morphology of terminal alveoli more closely than traditional semi-circular "grape cluster" representations [14, 15]. To simulate the deformation of the lung parenchyma tissue and the resulting oscillatory flow fields, the model implements a fluid-structure interaction (FSI) technique. In contrast to other models that use prescribed velocities and wall motions [10-13, 16-18], the current FSI technique uses tissue

motion to generate airflow within the alveolus and therefore provides a more accurate representation of negative pressure breathing dynamics. The FSI flow results are exported to a particle-tracking algorithm that calculates particle motion over time steps that are shorter than the time step used in the FSI simulation to capture rapid Brownian diffusion dynamics. Finally, the model reveals how several physical properties influence particle motion and it explores the relative importance of convection and diffusion at the alveolar scale

II. METHODOLOGY

A. Fluid-Structure Interactions (FSI)

A thoughtful approach to modeling alveolar dynamics starts with an understanding of breathing mechanics. At the beginning of each breath, the inspiratory muscles contract and the ribcage moves up and out while the diaphragm moves down. Tissue stresses transferred through the lung parenchyma expand the alveoli. The increase in alveolar volume establishes a sub-ambient pressure within the alveoli that drives air flow into the lungs. At the end of inspiration, airflow into the lung has equalized the internal and external pressures and flow ceases. As the inspiratory muscles relax, elastic recoil decreases alveolar volume and increases the alveolar air pressure. Air flows out of the lungs until the internal and external pressures are again equal. Thus, at the alveolar level, tissue deformation drives the flow field.

The direct relationship between tissue motion and airflow in the alveoli naturally suggests a fluid-structure interaction simulation technique. Although this approach is computationally intensive, it has several desirable features. Instead of arbitrarily imposing the wall motion, the model transmits loads through the tissues to the alveolar wall. In this model, tissue properties such as elasticity or viscosity influence wall motion, alveolar flow patterns, and particle pathways. Therefore, this coupled fluid-structure interaction (FSI) computational model represents an important step toward the realistic simulation of alveolar breathing mechanics.

The simulations employ the ADINA 8.2 [19] finite element (FE) package for the time-dependent FSI models. Each ADINA model has a fluid domain and a solid domain. Fluid flow is governed by the incompressible continuity and Navier-Stokes equations.

$$\rho \frac{\partial v_i}{\partial x_i} = 0 \tag{1}$$

$$\rho \frac{\partial v_i}{\partial t} + \rho v_j \frac{\partial v_i}{\partial x_j} = -\frac{\partial p}{\partial x_i} + \mu \frac{\partial^2 v_i}{\partial x_j \partial x_j} \tag{2}$$

Where ρ is the fluid density, μ is the fluid viscosity, v_i is the velocity vector, x_i is the position vector, t is time, and p is the fluid pressure. Tissue deformation in the solid domain is governed by a standard stress balance relationship and a Kelvin-Voigt viscoelastic constitutive relationship [19-21].

$$\frac{\partial \sigma_{ij}}{\partial x_j} = 0 \tag{3}$$

$$\sigma_{ij} = E\varepsilon_{ij} + \eta \frac{\partial \varepsilon_{ij}}{\partial t}, \text{ where } \varepsilon_{ij} = \frac{1}{2}\left(\frac{\partial d_i}{\partial x_j} + \frac{\partial d_j}{\partial x_i}\right) \tag{4}$$

Here σ_{ij} is the stress tensor, E is the Young's modulus, ε_{ij} is the strain matrix, η is the viscosity, and d_i is the solid displacement in a given direction. In ADINA, the viscoelastic material is formulated with a Prony-Dirichlet series with user-supplied coefficients [19]. (See Appendix A for additional details on modeling viscoelastic materials in ADINA.)

In the FSI models, the fluid and solid domains are coupled by satisfying the following three boundary conditions at the interface between the two domains.

$$d_i^f = d_i^s \tag{5}$$

$$n_j \sigma_{ij}^f = n_j \sigma_{ij}^s, \text{ where } \sigma_{ij}^f = -p\delta_{ij} + \mu\left(\frac{\partial v_i}{\partial x_j} + \frac{\partial v_j}{\partial x_i}\right) \tag{6}$$

$$n_i v_i = n_i \frac{\partial d_i^s}{\partial t} \tag{7}$$

Where d_i^f and d_i^s are the fluid and solid nodal displacements, n_j is the interface normal vector, δij is the Kronecker delta function, and σ_{ij}^f and σ_{ij}^s are the fluid and solid stress tensors. The kinematic condition in Eq. (5) requires equal displacements of the fluid and solid nodes at the fluid-structure interfaces. The dynamic condition in Eq. (6) specifies stress continuity between the fluid and solid domains. Finally, the fluid velocity condition in Eq. (7) is a no-slip boundary condition at fluid-solid interface.

An iterative solution scheme accounts for two-way coupling between the fluid and solid domain and solves Eqns. (1-4). For the first time step, Eqns. (1) and (2) are solved with the no-slip boundary condition in Eq. (7) for the flow velocities in the fluid domain and the fluid tractions, σ_{ij}^{f}, at the fluid-structure boundary. The calculated values of σ_{ij}^{f} are then used as boundary conditions in Eqn. (6) to solve Eqns. (3) and (4) for deformations in the solid domain. These deformations result in a new shape for the fluid domain and the ADINA solution routine checks whether the kinematic and dynamic conditions, Eqns. (5) and (6), are satisfied. If these conditions are not satisfied, the solver repeats the fluid and solid computations with the updated traction and displacement information. To maintain stability and to speed the approach to convergence, the solver employs displacement and stress relaxation factors when passing boundary information between the fluid and solid domains. When the solver reaches a converged solution, it stores the information and moves to the next time step. ADINA uses an Euler backward time stepping algorithm, which is first order accurate and implicit.

B. Model Definition

Meaningful FSI simulations arise from physiologically-motivated computational domains. Although typical artists' renditions of the deep lung morphology show little alveolar interconnectivity [22], neighboring alveoli actually share thin, flat walls and usually have fluid dynamic and structural connectivity [23, 24]. Based on this observation, the alveolar sacs in this study are modified 2-D hexagonal honeycombs (see Fig. 1). The final model, which was generated in the Rhinoceros 3.0 CAD package, has three neighboring alveolar sacs that deform when an oscillatory load is applied to the surrounding tissue as shown in Fig. 1. When the model is not loaded, it has an inlet duct diameter of 200 μm, and an alveolar entrance length of 100 μm. These dimensions are consistent with typical alveolar ducts and sacs in adult human lungs [23, 25, 26]. The corners of each alveolus are filleted to mimic the rounded concave corners produced by the liquid lining layer present in the lungs [27] and to reduce stress concentrations in the solid

domain. Although this geometry accounts for the shape seen by the air, the current models do not directly simulate surface tension dynamics within the liquid layer.

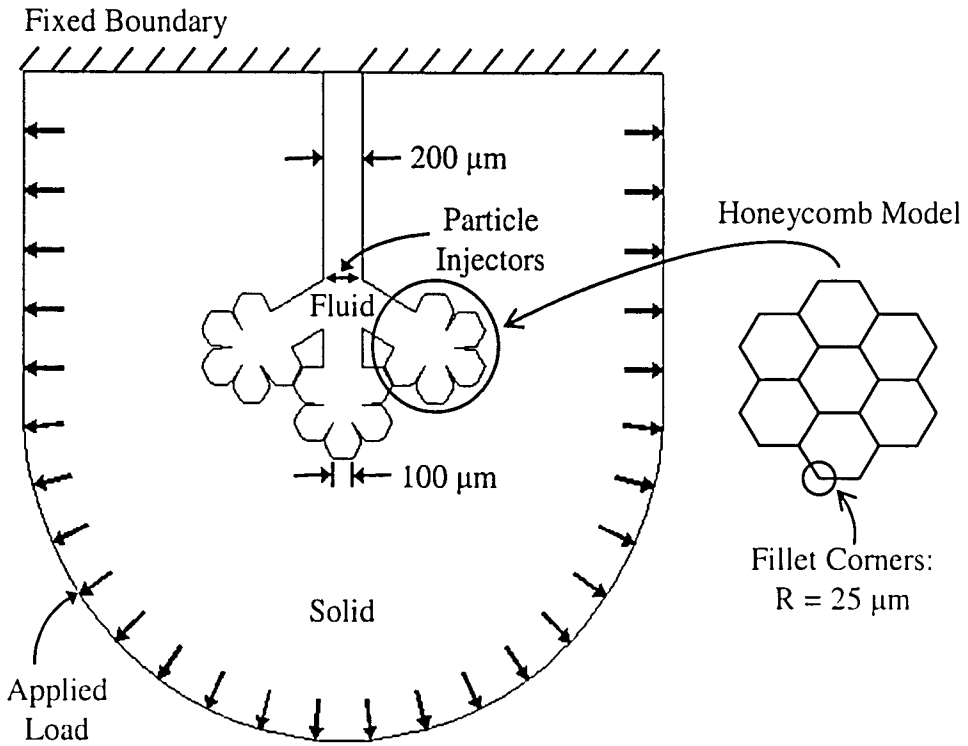

Fig. 1 Model schematic showing applied loads and characteristic dimensions.

The next step in the modeling process is to discretize the fluid and solid model domains. The solid mesh consists of 7-node triangular plane-strain elements. To maintain structural rigidity in the inlet duct, the model uses 3-node plane-strain isobeam elements along the walls of the inlet channel. There are 9,068 total elements and 27,231 nodes in the solid model. The fluid mesh contains 9,643 3-node triangular elements and 5,163 nodes. (See Appendix B for mesh pictures and element size information.) Although the solid elements have more nodes than the adjoining fluid elements, the FSI solver interpolates the fluid's nodal displacements from the solid mesh and the interface tractions for the solid nodes from the fluid mesh.

The parameter values for the tissue stiffness, E, and the magnitude of the applied load are selected to generate physiological flow rates. To estimate these flow rates, assume that the

change in lung volume during breathing occurs primarily in the alveolar sacs. As a result, the alveolar expansion can be calculated based on the tidal breathing volume, V_{TB}. As described in the Appendix C, a V_{TB}=500 ml yields an 8% change in alveolar radius during each breath. To match these 8% displacements, the models specify baseline values for the tissue parameters: E=10,000 dyn/cm^2 and η=0 g/cm-s. Varying the applied tissue load until the calculated wall displacements match the 8% alveolar expansion ratio isolates the appropriate load/stiffness ratio. Note that the final value for the applied load is 500 dyn/cm^2. This baseline case produces inlet flow rates that correspond with the values reported by Darquenne [11] for the equivalent Weibel generation.

From the baseline case discussed above, the simulations include a range of system properties to account for local tissue variations, disease states, breathing patterns, and particle types. Table I shows the baseline values and the parameter ranges used in this study. In all cases, tissue density was set at 0.28 g/cm3 [28]. Variations in E correspond to a range of disease states in which the lung parenchyma is more or less stiff than normal tissue [29]. The chosen range of η makes the ratio of stress relaxation time to breathing period vary from approximately 0.15 to 1. This range is sufficient to assess the influence of viscoelasticity by varying the time delay of the tissue response. The range of λ_{TB} includes the spectrum of typical breathing rates. Finally, the distribution of particle sizes represents aerosol exposure conditions ranging from bacteria and viruses to pharmaceuticals and dust.

Parameter	Baseline	Range
Tissue Elasticity	E = 10,000 dyn/cm^2	7,500 < E < 12,500
Tissue Viscosity	η = 0 g/cm-s	5,000 < η < 15,000
Breathing Period	λ_{TB} = 5 sec	5 < λ_{TB} < 15
Particle Diameter	d_p = 1 μm	0.1 < d_p < 5

Table I Value ranges for solution parameters used in the finite element model.

C. Particle Tracking

This study investigates the behavior of a dilute suspension of micron-sized particles with no particle-particle interactions. In addition, this work assumes that the motion of these small particles does not influence the fluid flow calculation. Based on these assumptions, the first step is to perform the full FSI simulation and calculate fluid velocities at all time steps. Next, the fluid solution variables must be extracted from the FSI simulation in time increments of $\Delta t = 0.9375$ sec. Note that this corresponds to 16 time steps per breathing period when $\lambda_{TB} = 15$ sec. Finally, a MATLAB [30] post-processing routine integrates the following differential equation of particle motion in two dimensions.

$$\frac{dv_i^p}{dt} = F_D\left(v_i - v_i^p\right) + \frac{g_i\left(\rho_p - \rho\right)}{\rho_p} + F_i^B \tag{8}$$

Here, v_i^p and v_i represent particle and fluid velocities, ρ_p and ρ represent particle and fluid densities, F_D is the drag force on the particle and g_i is the gravity vector. Equation (8) is known as the Langevin equation and represents a balance of inertia, drag, gravity, and Brownian forces [31]. The tracking algorithm uses a Crank-Nicolson integration scheme that is second-order accurate and implicit (see Appendix D for detailed formulation).

In these simulations, intermolecular slip may be significant due to the small size of the particles. A modified Stokes' formulation for the drag term, F_D, accounts for this effect.

$$F_D = \frac{18\mu}{d_p^2 \rho_p C_c} \tag{9}$$

$$C_C = 1 + \frac{2\lambda}{d_p}\left(1.257 + 0.4\exp\left(-1.1 d_p / 2\lambda\right)\right) \tag{10}$$

Here μ is the fluid viscosity, C_C is the Cunningham slip correction factor [31, 32], and λ is the molecular mean free path of air. The Brownian term, F_i^B (Eq. 11) is a stochastic random vector defined in terms of the particle and fluid properties and the solution time step [32].

$$F_i^B = \zeta_i \sqrt{\frac{\pi S_0}{\Delta t}} \tag{11}$$

$$S_o = \frac{216 \upsilon k T}{\pi^2 \rho d_p^{\,5} \left(\frac{\rho_p}{\rho} \right)^2 C_C} \tag{12}$$

Here, ζ_i is a zero-mean, unit-variance Gaussian random vector, S_o is the amplitude of the white noise process, υ is the kinematic viscosity of the air, $k = 1.38 \times 10^{-16}$ is the Boltzman constant, and T is the temperature of the air. In this study, all gas properties are at body temperature, $T = 37°C$.

As a validation for the particle motion algorithm, the root mean squared (RMS) displacement of a Brownian particle in an infinite quiescent medium can be compared to the theoretical diffusion predicted by Einstein [33].

$$RMS = \sqrt{\overline{z^2}} = \sqrt{2Dt} \tag{13}$$

Here, the diffusion constant, D, includes the Cunningham slip correction factor [34].

$$D = \frac{kTC_C}{3\pi\mu d_p} \tag{14}$$

For a particle with diameter $d_p = 0.1$ μm, Fig. 2 shows the simulated Brownian RMS displacement approaching the theoretical value as the time step, Δt, decreases. This convergence study indicates minimal differences between the solutions for $\Delta t = 0.001$ and 0.0001 sec. Therefore, this study specifies $\Delta t = 0.001$ for all simulations.

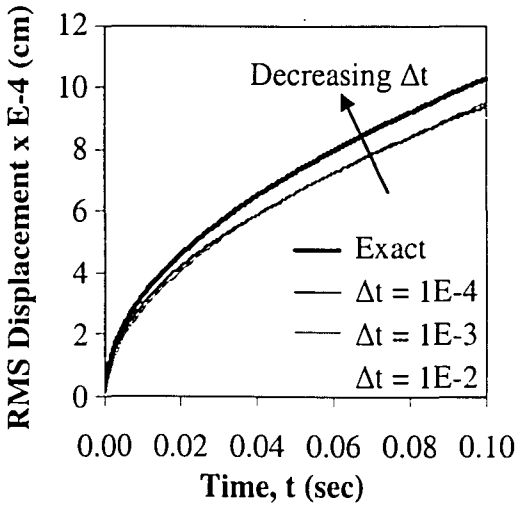

Fig. 2 As time step size decreases, the simulated RMS particle displacement approaches the theoretical result of Equation 13.

D. Statistical Analysis

This study is concerned with the effect of particle diameter, tidal breathing period, and tissue elasticity/viscosity on alveolar particle transport. However, the stochastic Brownian force term in the particle equation of motion can produce significant variations between particle paths emanating from the same initial location. Thus, it is not possible to draw conclusions about the general behavior of particles under a certain set of conditions without a statistical analysis based on repeated measurements. Therefore, the analysis requires a series of FSI simulations over a range of tissue models and breathing rates. Specifically, there are 7 tissue models (i.e. different values for E and η) and 4 breathing periods for a total of 28 different cases or treatment groups. The time-dependent flow data is extracted from the FSI simulation for each treatment group and the data goes to the MATLAB particle tracking routing. The MATLAB routine defines an array of 21 particle injectors where the airway divides into the three alveolar sacs (see Fig. 2). For all 28 treatment groups, the MATLAB routine computes 10 particle paths from each of the 21 injectors. Finally, this calculation must be repeated for the seven different particle diameters. As a result, the total number of particle pathways computed in this study is 41,160.

For the statistical analysis, three outcome parameters measure how far the particles travel, how many particles land on the walls, and how long they take to land on the walls. A two-factor analysis of variance (ANOVA) identifies any statistically significant variations in the outcome parameters within the 28 treatment groups. A least significant difference (LSD) post hoc test identifies any statistically significant differences between specific treatment groups. Significance for these tests is set at $P < 0.05$.

III. RESULTS

The particle tracking results fall into two categories: Non-Brownian (part A) and Brownian (part B). Particle behavior after injection has three characteristic measurements: displacement from the injection location, Δ_p, impaction rate, R_{imp}, and time to impaction, t_{imp}. In the case of Non-Brownian particles, there is no random force component, so there are no repeated measurements for R_{imp}, t_{imp}, and Δ_p. The Brownian particle results include statistics based on 1,470 particle paths in each of the 28 treatment groups.

A. Non-Brownian Particles

A.1—Symmetric Tissue Properties

The behavior of micron-sized particles without the influence of Brownian diffusion or gravity provides a convenient visualization tool for understanding the transient flow patterns in the alveolar structure. Figure 3 shows the paths traversed by 1-μm particles over the course of 10 breathing cycles. Due to the orientation of the three alveolar sacs within the tissue, the central sac generates slightly higher flow rates, as evidenced by particle drift toward the system centerline. Except for particles injected within 1 μm of the moving walls, the particles remain entrained in the fluid and do not impact the walls.

Non-Brownian particles have limited wall impaction, so the only useful metric for quantifying particle behavior is displacement from the injection location, Δ_p. At every point along the particle's path, the tracking routine computes the particle's straight-line distance from the injector. Note that only the maximum distance a particle travels from its injector while it remains entrained in the airflow is used to calculate Δ_p. Figure 4 shows Δ_p profiles for the three models with different tissue elastic moduli. Note that only purely elastic tissue models (i.e. viscosity, η=0) are shown in Fig. 4 and that each curve represents the average of four treatment groups with different breathing periods. Clearly, particles injected near the high-velocity centerline travel farther into the system. Particle paths that pass near a carina (shown in Figure 3)

have reduced displacements. These results suggest that decreasing E increases particle propagation depth.

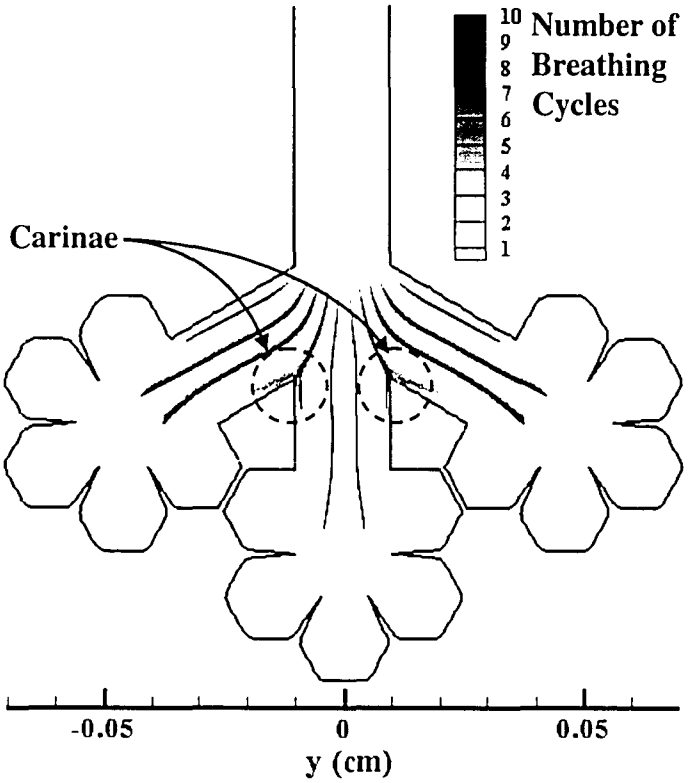

Fig. 3 Non-Brownian particle paths for $d_p = 1$ μm. Shaded areas show the region traversed by each particle and the shading indicates particle position after each inspiration-expiration cycle.

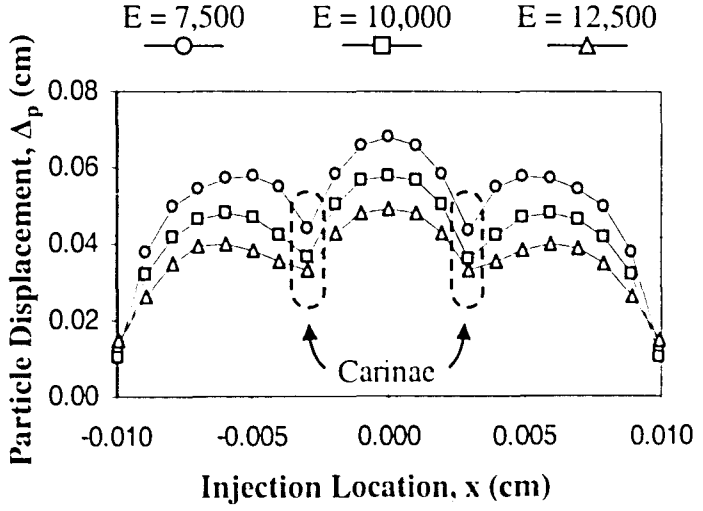

Fig. 4 For non-Brownian particles, propagation depth depends on the local velocity at the injection location and the downstream airway configuration. Particles that pass near a carina do not travel as far into the system.

Another measurement of the influence of tissue properties on particle propagation is the maximum particle displacement, $(\Delta_p)_{max}$, as a function of breathing period for various values of E and η (see Fig. 5). Note that the data in Fig. 5a uses a constant η=0 g/cm-s while the data in Fig. 5b uses a constant E=10,000 dyn/cm^2. An ANOVA with LSD post hoc analysis confirms that E, η, and λ_{TB} all have a statistically significant effect on particle propagation depth ($P < 0.001$ between all treatment groups). Specifically, increasing the elastic modulus, E, or the viscosity, η, reduces particle displacements $(\Delta_p)_{max}$. These results are for non-Brownian particles, so the trends represent the contribution of convection forces only.

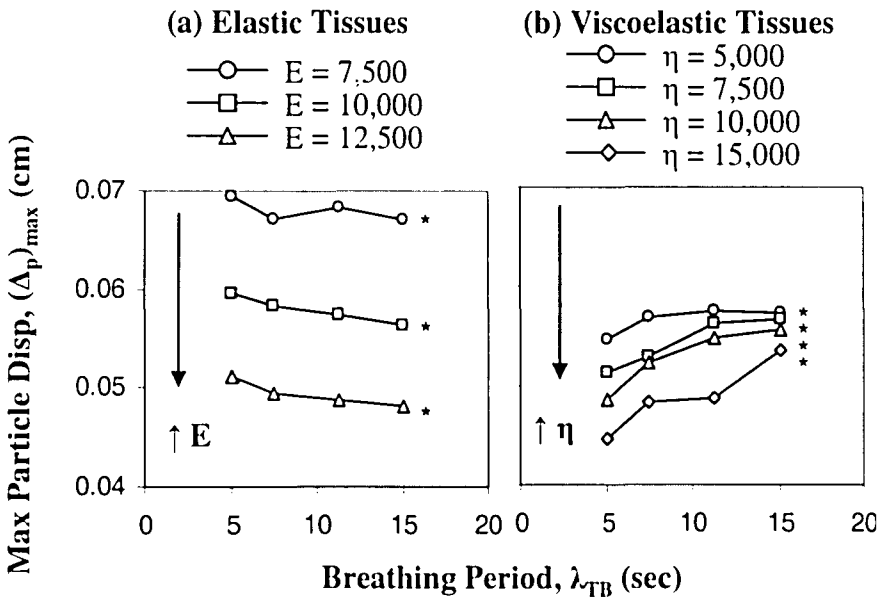

Fig. 5 For non-Brownian particles, increasing E and η reduces particle propagation into the system. Symbols denote statistically significant differences due to tissue model.

A.2—Asymmetric Tissue Properties

The computational mesh for the solid domain has three distinct zones, as shown in Fig. 6. Each zone can have different solid properties and this feature illustrates the effects of asymmetric tissue stiffness on particle transport. Zones 1 and 2 have the baseline stiffness, E=10,000 dyn/cm^2, and zone 3 is twice as stiff, so that $E_3=2E_1$. Figure 7 shows non-Brownian particle paths through the resulting asymmetric flow field. Particles that pass into the lower-velocity flows in the stiffer zone do not propagate as deeply into the system.

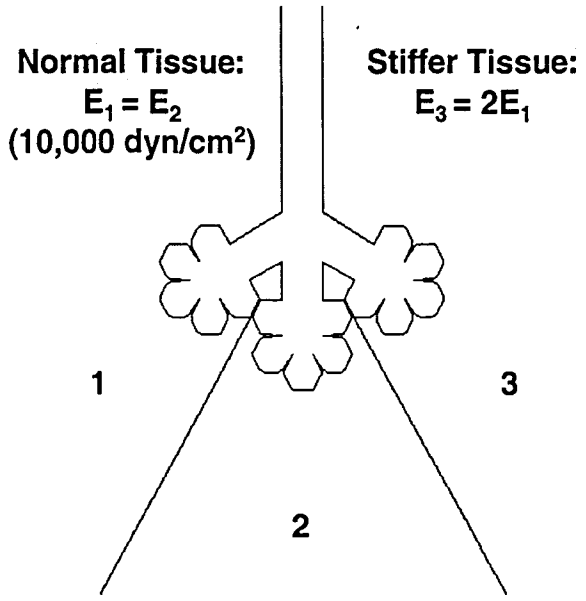

Fig. 6 Three separate tissue zones can have independently-defined solid properties. For the asymmetric study, the zone 3 on the right is twice as stiff as zones 1 and 2.

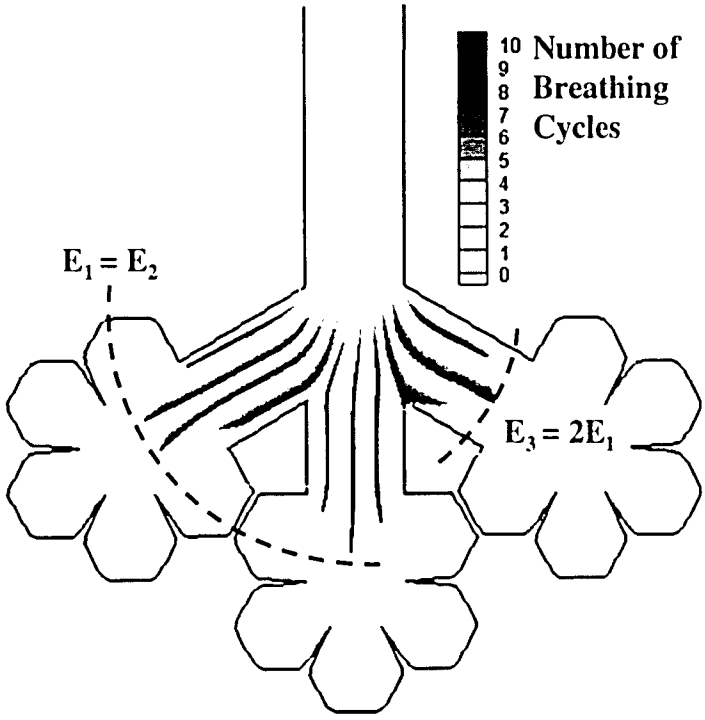

Fig. 7 The alveolar sac on the right is surrounded by stiffer tissues than the other two sacs. Particles do not travel as deeply into regions surrounded by stiffer tissues.

B. Brownian Particles

B.1—Impaction Rate and Time to Impaction

In this study, when a particle's computed trajectory causes it to pass out of the fluid domain, the tracking routine assumes it impacts the wall at that location. Particle impaction rate, R_{imp}, is the percentage of particles injected into the flow that impact the walls within ten breathing cycles. The time to impaction, t_{imp}, measures how much time a particle spends in the fluid before passing out of the domain. These measurements illustrate effect of breathing period, λ_{TB}, and particle diameter, d_p, on R_{imp} and t_{imp} for all 28 treatment groups.

Figures 8 and 9 show how R_{imp} and t_{imp} vary as a function of particle size at different breathing frequencies. Each curve represents the average values obtained in seven treatment groups where each group has a unique combination of tissue mechanical properties (i.e. different E and η) and the same breathing period. The standard deviation bars reflect the range of results obtained in the different treatment groups and therefore include elastic and viscoelastic formulations. When $d_p \leq 1$ μm, all particles impact the walls, so there is no dependence on tissue type or breathing period. As particle size increases, the impaction rate, R_{imp}, decreases and the time to impaction, t_{imp}, increases. For larger particles, R_{imp} and t_{imp} increase during slower breathing (higher λ_{TB}). Figures 10 (R_{imp}) and 11 (t_{imp}) visualize these trends for d_p = 2.5 and 5 μm. Each curve represents the average of all elastic and viscoelastic treatment groups. A between-groups ANOVA including the 28 elastic and viscoelastic treatment groups indicates that breathing period has a significant effect on both R_{imp} and t_{imp}.

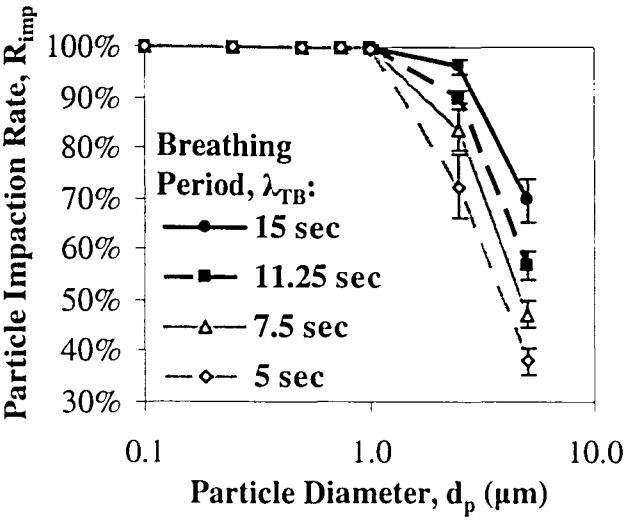

Fig. 8 Average particle impaction rates for all tissue models. R_{imp} drops sharply above d_p=1 μm; faster breathing cycles magnify this effect. Error bars denote standard deviation.

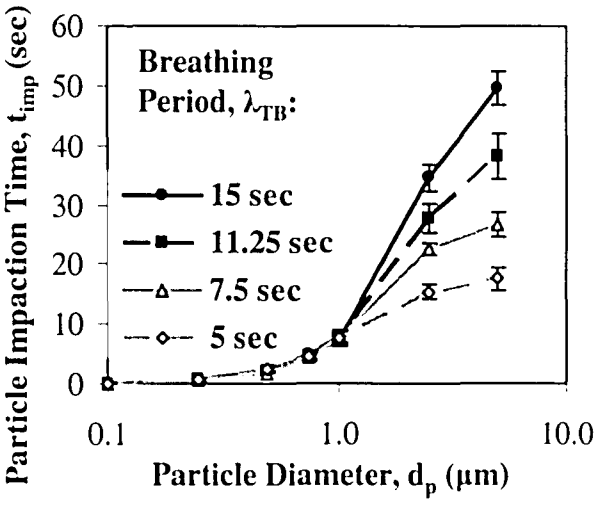

Fig. 9 Average particle time to impaction for all tissue models. Impaction time is proportional to the length of the breathing cycle. Error bars denote standard deviation.

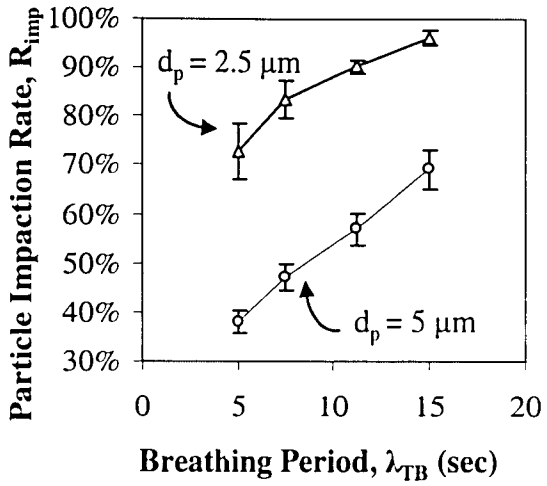

Fig. 10 Impaction rate increases during slower breathing (higher λ_{TB}) for all tissue models. Error bars denote standard deviation. The effect of breathing period is statistically significant between all treatment levels.

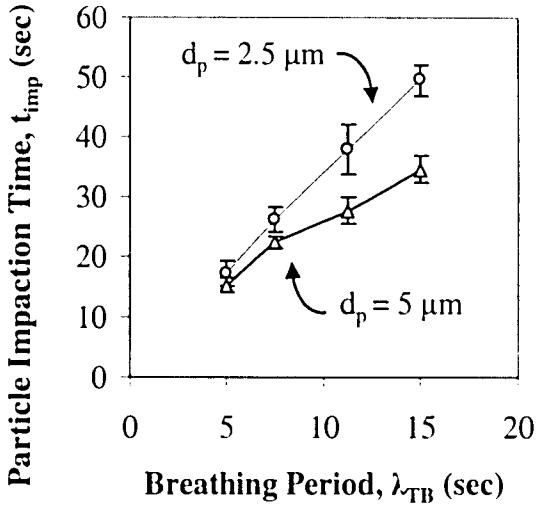

Fig. 11 Time to impaction increases during slower breathing (higher λ_{TB}) for all tissue models. Error bars denote standard deviation. The effect of breathing period is statistically significant between all treatment levels.

The simulations also contain information on the relative importance of tissue mechanical properties on particle impaction rate. Separate ANOVA calculations for the 12 elastic and 16 viscoelastic treatment groups yield the results in Table II.

		E		η	
	d_p	P	Significant?	P	Significant?
R_{imp}	2.5	0.001	✓	0.137	X
	5	0.027	✓	0.462	X

Table II Tissue elasticity, E, has a statistically significant effect on particle impaction rate, but viscosity, η, does not.

Tissue elasticity, E, has a statistically significant effect on R_{imp}, while tissue viscosity, η, does not. Figure 12 shows how R_{imp} varies as a function of E where each curve represents the average of all breathing periods. In this case, stiffer tissues have higher R_{imp}. The LSD post-hoc analysis reveals which treatment groups are significantly different (see Fig. 12).

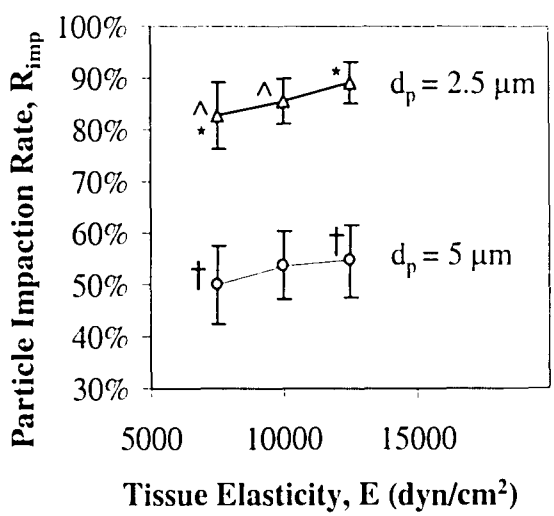

Fig. 12 Increasing tissue elasticity increases the particle impaction rate. Error bars denote standard error. Symbols denote significantly different treatment levels.

B.2—Particle Displacement

Figure 13 shows how particle displacement, Δ_p, varies as a function of the injection location for Brownian particles in different tissue mechanical models (similar information is shown in Fig. 4 for non-Brownian particles). For both elastic and viscoelastic tissues, there is a strong parabolic correlation between the injection location and the particle's propagation depth.

Specifically, particles injected into the high-velocity flow near the centerline propagate much deeper into the alveolar sac than particles injected in the low-velocity regions near the walls.

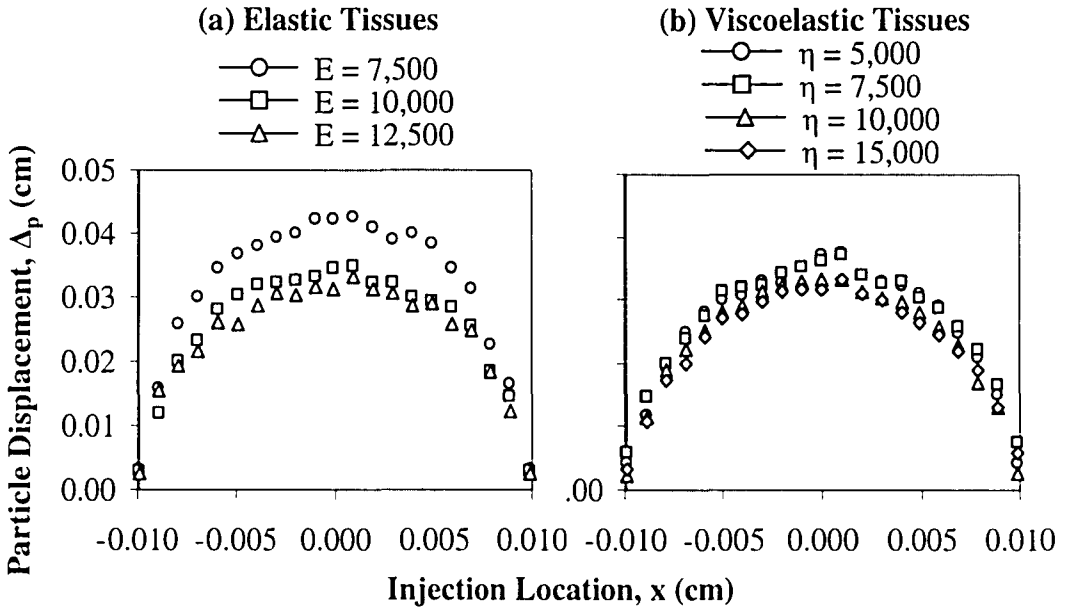

Fig. 13 Decreasing elasticity, E, increases particle displacement from the injector location, Δ_p. Changing viscosity, η, has no significant effect.

An ANOVA analysis between the 12 elastic treatment groups and between the 16 viscoelastic treatment groups reveals the significance of changing tissue models. Elasticity, E, has a statistically significant effect on Δ_p ($P = 0.014$), where increasing E decreases Δ_p (see Figure 13a). However, viscosity does not significantly influence Δ_p ($P = 0.548$) as shown in Figure 13b.

C. Brownian Particles with Gravitational Sedimentation

The Langevin equation (Eq. 8) contains terms for convection, Brownian diffusion, and gravitational sedimentation. Gravitational settling can be a significant particle deposition mechanism, especially for the larger, more massive particles in the study. However, including gravity introduces orientation dependency in the results. Figure 14 compares sample particle paths for a range of particle sizes. The smaller particles (on the left in Fig. 14) experience more Brownian diffusion, while the larger particles (on the right in Fig. 14) experience more gravitational sedimentation.

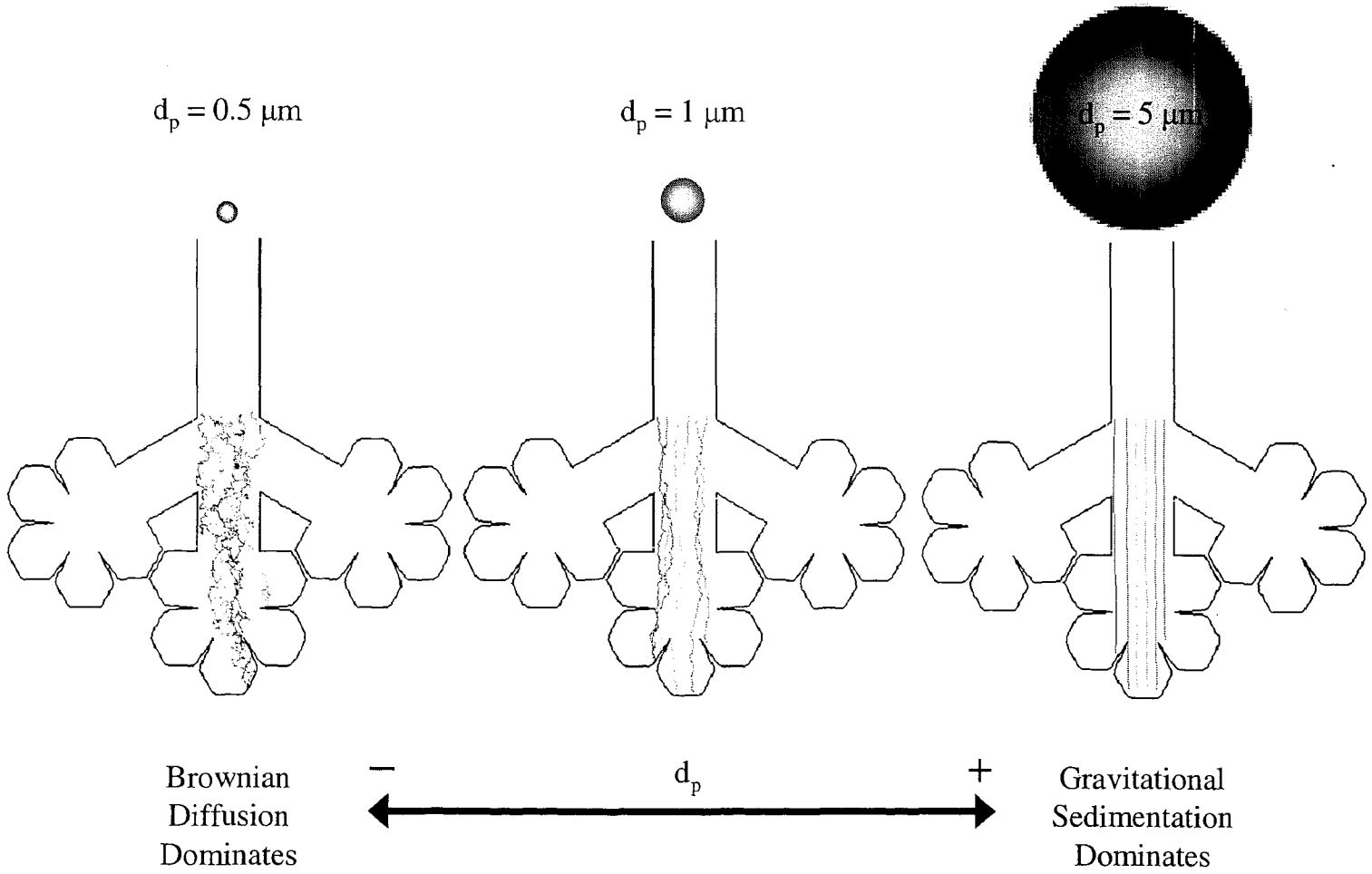

Fig. 14 Brownian diffusion is the dominant deposition mechanism for smaller, lighter microparticles. Gravitational sedimentation dominates for larger, heavier particles.

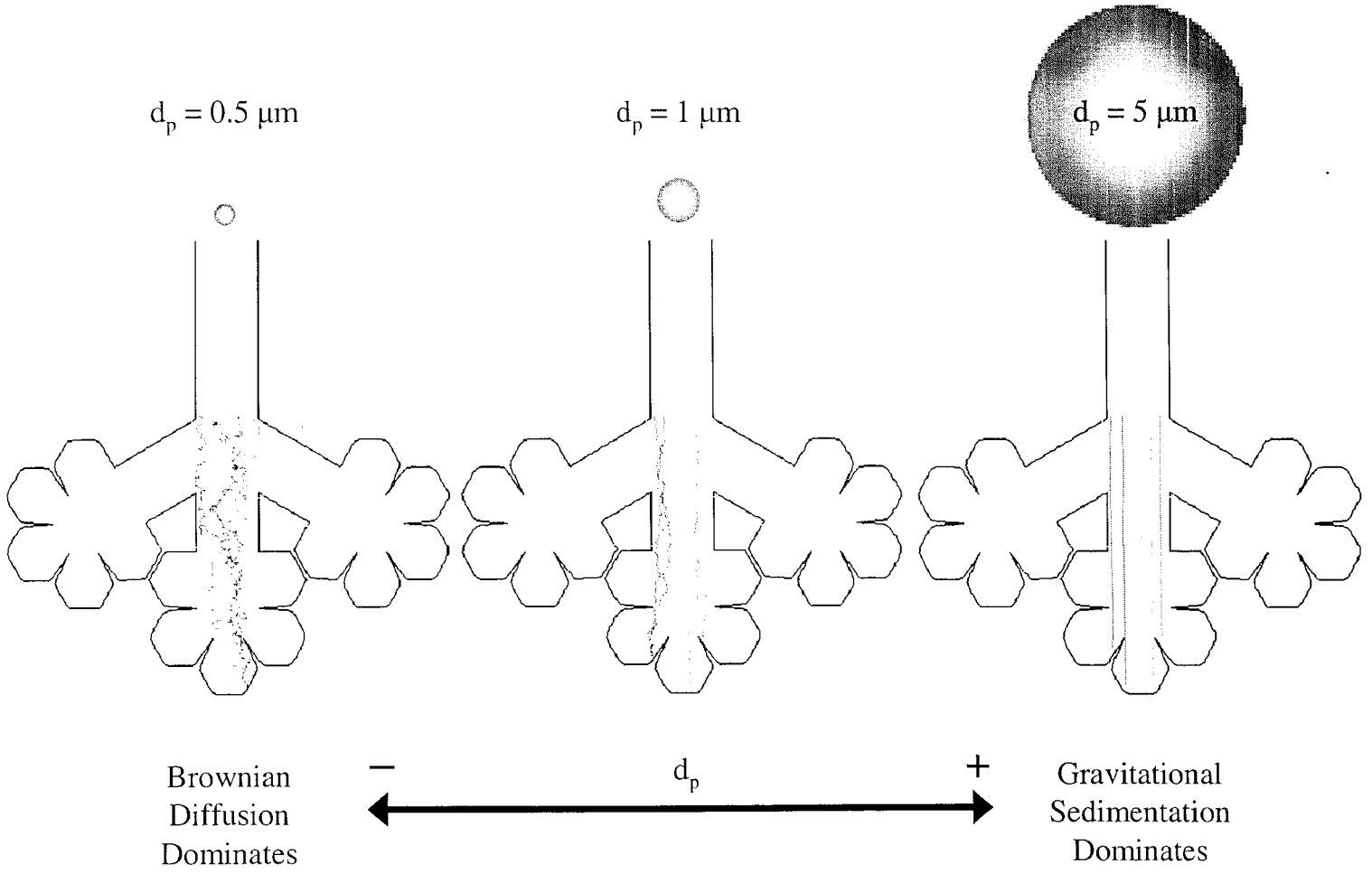

Fig. 14 Brownian diffusion is the dominant deposition mechanism for smaller, lighter microparticles. Gravitational sedimentation dominates for larger, heavier particles.

The particle impaction time can quantify the dominance of gravitational sedimentation. Figure 15 compares the average t_{imp} results for all treatment groups with and without gravity. As expected, gravitational sedimentation becomes increasingly dominant for larger particles.

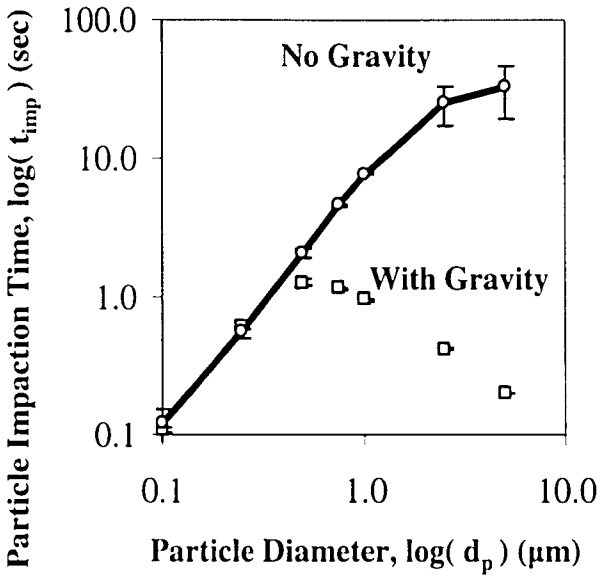

Fig. 15 Gravitational sedimentation produces low impaction times for large particles that experience little Brownian diffusion. Error bars denote standard deviation.

IV. DISCUSSION

Prior to this study, other investigators studied various aspects of alveolar dynamics, but none of them simultaneously treated all of the modeling challenges outlined in this study: alveolar interconnectivity, tissue-driven wall motion, and Brownian-diffusive particle dynamics. The unique contribution of this study is the successful coupling of fluid-structure interactions in a physiologically-motivated alveolar geometry with an efficient particle tracking algorithm. This synthesis of tools allows for an analysis of how geometry, tissue mechanical properties, and convection/diffusion transport mechanisms influence microparticle transport in the deep lung.

A. Geometry Effects

The shape and orientation of the alveolar sacs within the tissue can determine how deeply particles propagate into the system. Non-Brownian particles that pass near a carina have reduced displacements because they become trapped in the slower flow near the walls (see Fig. 4). However, the displacements calculated for particles with Brownian motion do not reflect the presence of the carinae. For the Brownian particles, the carinae do not influence particle propagation depth because particles randomly cross streamlines and do not necessarily become entrained in the slow flow near these geometry features. This result suggests that diffusional transport overwhelms any potential geometry effects at these small scales.

B. Tissue Effects

Tissue properties influence particle behavior by altering the system's response to loading. In the case of elastic tissues, increasing the stiffness (higher E) restricts wall displacement and generates lower-velocity flows. Lower-velocity flow patterns decrease the convective forces that pull particles farther into the alveolar sacs. As a result, increasing the elastic modulus, E, reduces particle displacements, Δ_p (see Figs. 4, 5a, and 13a). Increasing E also results in a higher particle impaction rate, R_{imp} (see Fig. 12). This relationship between E and R_{imp} is due to the magnitude of convective forces decreases with increasing E. As a result, the influence of Brownian

diffusion, which is responsible for particles crossing streamlines and impacting on the walls, is magnified at large E. This relationship between convection and diffusion is further analyzed below.

C. Convection vs. Diffusion Dominance

Although several authors have investigated the transport of micron-sized particles in the deep lungs, the relative importance of convection and diffusion forces is not well established. For example, Tsuda et al. [10] included Brownian forces when tracking particles ranging from 0.05 to 5 μm in alveolated ducts, while Darquenne's investigations [17] neglected Brownian diffusion for particles larger than 0.5 μm in diameter. Haber et al. [13] also neglected Brownian dynamics but acknowledged that it may be important for alveolar flows. One possible source of confusion regarding the importance of Brownian diffusion arises from the fact that Brownian-scale motions seem irrelevant for particles traveling through relatively large structures. However, these small motions become increasingly significant as the characteristic size of the domain approaches the displacements generated by diffusion alone.

The impaction rate data obtained from these simulations supports the inclusion of Brownian dynamics for microparticle transport in pulmonary alveoli. From Fig. 8, it is evident that $d_p = 1$ μm is a critical size that divides the results into two regimes. Specifically, for $d_p < 1$ μm, Brownian diffusion alone carries particles out of the domain and therefore 100% of injected particles impact the walls, regardless of convective forces in the system. This result can be explained by considering Einstein's theoretical diffusion relationship (Eq. 13), which is plotted in Fig. 16 for different particle diameters. The inlet duct diameter is system's characteristic length, l_c, and it has been plotted as a horizontal reference scale on Fig. 16. Comparing the l_c to the RMS displacements indicates that that Brownian diffusion alone will carry smaller particles ($d_p < 1$ μm) beyond the physical limits of the system. As a result, 100% of the particles with $d_p < 1$ μm become impacted on the wall.

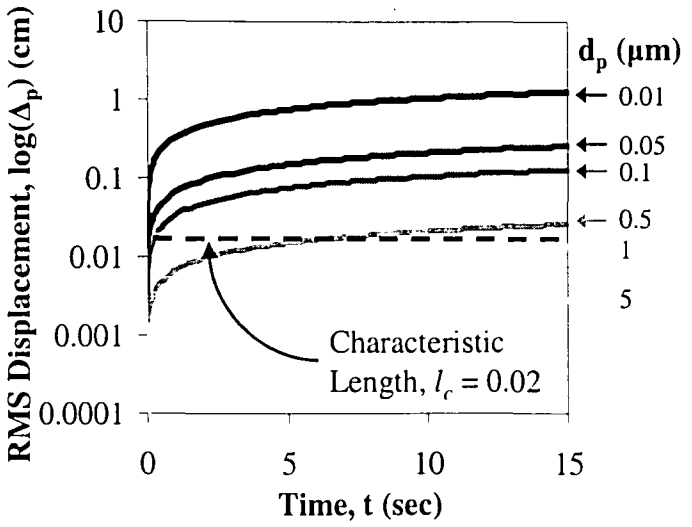

Fig. 16 Einstein's diffusion relationship (Eq. 13) for a range of particle diameters. The characteristic length, l_c, delineates the alveolar boundary. During one slow breathing cycle, diffusion alone will carry the smaller particles out of the domain.

For particles larger than 1 μm, impaction rates decrease significantly with increasing particle size (see Fig. 8). Larger particles have more mass, experience larger drag forces and are therefore easier to carry with the bulk convective flow. As a result, diffusion is less significant for these larger particles. Since diffusion is required for particles to cross streamlines and impact on the walls, impaction rates decrease for large particles. Fig. 8 also demonstrates that high breathing frequencies, i.e. low breathing periods (λ_{TB}), result in lower impaction rates. At high breathing frequencies, convective forces are elevated, diffusion is less significant and therefore particle impaction rates decrease.

The data in Figs. 8 and 9 suggests that the ratio of convection to diffusion strongly influences particle behavior in this system, so a dimensionless analysis is a useful tool for investigating the relative importance of convection and diffusion. For the data obtained in each particle path, t_{imp} can be divided by λ_{TB} to calculate the number of breathing cycles to impaction, NC_{imp}. Next, the particle diameters in each simulation can be converted to their equivalent Peclet number, or dimensionless convection-diffusion ratio.

$$Pe = \frac{(d_w)_{max} l_c}{\lambda_{TB} D} \tag{15}$$

Equation (15) gives the Peclet number in terms of the maximum alveolar wall displacement, $(d_w)_{max}$, duct diameter, l_c, and diffusion constant, D, as given in Eq. (14). Figure 17 shows NC_{imp} as a function of Pe for all elastic and viscoelastic treatment groups. In this format, the data collapses to a single relationship.

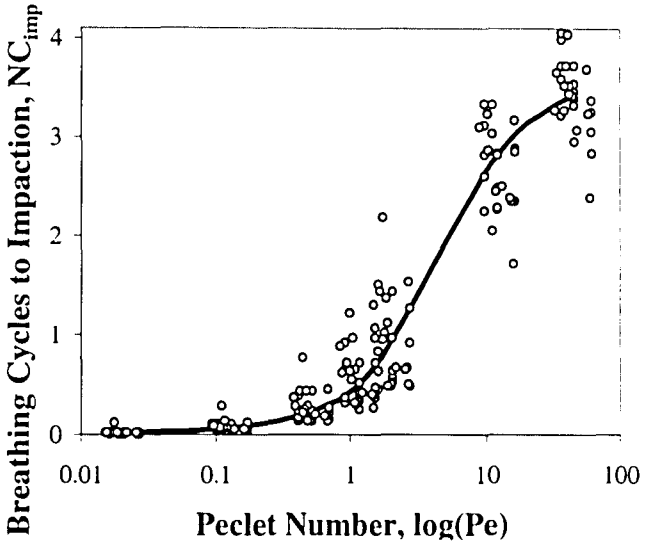

Fig. 17 After dimensional analysis, the data from Fig. 7 collapses to a single curve. The number of breathing cycles to impaction, NC_{imp}, does not depend on tissue type or breathing period.

An ANOVA analysis confirms that NC_{imp} does not have a statistically significant dependence on the tissue type (P = 0.247) or on breathing period (P = 1.000). Thus, the number of breathing cycles before impaction is only a function of the Peclet number, or the convection/diffusion ratio. This result indicates that Brownian motions play a major role in the transport of sub-micron particles inside small structures such as pulmonary alveoli. In addition, convection becomes increasingly dominant as particle size and bulk fluid velocity increase. Finally, the relative importance of convection and diffusion can be accurately ascertained with the dimensionless Peclet number.

The convection/diffusion ratio result helps explain why larger particles have higher standard deviations for t_{imp} in Figs. 9 and 15. Larger particles experience more convective forces, so their time to impaction is more dependent upon the initial velocity at the injection location. Some particles are injected into slow flow near the walls and some are injected into fast flow near the centerline. Less Brownian diffusion also means that particles cross fewer streamlines, so impaction times for the large particles show a stronger correlation with injection location, and hence, a wider standard deviation than for small particles.

D. Model Limitations

As with any computational model, this study does not include all of the physical phenomena that may affect particle transport in the pulmonary alveoli. Although this study briefly examines the effect of gravity on particle transport in this system, most of the results neglect sedimentation effects. This assumption isolates the effects of convection and diffusion in an orientation-independent domain. Particles in real alveoli do experience gravitational settling, but this study leaves a thorough comparison of gravitational, diffusive, and convective effects for a future investigation. This study also recognizes the limitations involved in approximating alveolated sacs as 2D structures. During breathing, these tortuous pathways experience cyclical out-of-plane collapsing and unfolding. In addition, a thin liquid layer covers the alveolar capillary boundary and surface tension forces within that layer may be important for understanding breathing mechanics at the alveolar level [35]. Finally, true breathing patterns may not be purely sinusoidal as described here. Irregular breathing, including breath-holding, may be of particular interest for deep lung aerosol applications.

V. CONCLUSIONS

In summary, this study developed a fluid-structure interaction model for alveolar breathing mechanics and a particle tracking routine to simulate particle motion in small alveolar sacs. The models simulated ten inspiration-expiration cycles for a range of particle sizes, breathing rates, and tissue mechanical properties. The results compared 28 treatment groups defined by breathing rate and the elastic and viscoelastic properties of lung parenchyma tissue.

For non-Brownian particles, particle impaction on the walls was negligible. Particle displacement from the injection location depended on the local fluid and downstream flow conditions. Particles injected into the high-velocity flow near the centerline traveled deep into the system. Particles that passed near the carinae, or airway division points, did not travel as far because of slow near-wall flow patterns (Fig. 4). Increasing the tissue elasticity decreased particle displacement because smaller wall displacements generate slower flows and less convection-driven particle motion (Fig. 5a). Increasing the viscosity also increased particle displacement because higher-viscosity tissues experience smaller wall displacements (Fig. 5b).

For the Brownian particles, an ensemble average of 1,470 particles paths in each of the 28 treatment groups provided three metrics for evaluating particle behavior.

1. *Particle Displacement:* Increasing tissue elasticity decreased particle displacement because the stiffer tissues produced less wall motion, lower flow velocities, and smaller convection forces (Fig. 13a). This trend can also be observed when tissue properties are asymmetric (Fig. 7). Tissue viscosity had no statistically significant effect on particle displacement (Fig. 13b).
2. *Particle impaction rate:* Impaction rate increased during slower breathing (Figs. 8 and 10). Stiffer tissues had higher impaction rates (Fig. 12) because convection forces decreased and Brownian diffusion dominated.

3. *Time to impaction:* Although the time to impaction increased during slower breathing (Fig. 11), the number of breathing cycles to impaction depended only on the Peclet number and was consistent for all breathing rates and tissue types (Fig. 17).

Einstein's theoretical diffusion relationship was employed to assess the importance of Brownian diffusion in alveolar-scale geometries. When the characteristic size of the structure was the same order of magnitude as the diffusion-driven displacement, Brownian diffusion became a critical deposition mechanism (Fig. 16). Also, as particle size increased, gravitational sedimentation became increasingly significant (Fig. 14). These results suggest that Brownian diffusion and gravitational sedimentation play a significant role in the dispersion and deposition of fine aerosols in pulmonary alveoli and should be included in the simulations of microparticle transport at the alveolar scale.

NOMENCLATURE

C_C = Cunningham slip correction factor

D = Brownian diffusion constant

d_i = displacement vector

d_p = particle diameter

$(d_w)_{max}$ = maximum alveolar wall displacement

E = Young's modulus

F_i^B = stochastic Brownian term

F_D = drag force on a particle

g_i = gravity vector

k = Boltzman constant = 1.38×10^{-16}

l_c = characteristic length (inlet duct diameter)

NC_{imp} = number of breathing cycles to impaction

n_j = FSI interface normal vector

p = fluid pressure

Pe = Peclet number

R_{imp} = particle impaction rate

RMS = root mean squared displacement

S_o = amplitude of the white noise process

T = temperature of the air

t = time

t_{imp} = time to impaction

v_i = velocity vector

V_{TB} = tidal breathing volume

x_i = position vector

Δ_p = particle displacement from injection location

Δt = time step in FSI simulation

δij = Kronecker delta function

ε_{ij} = strain matrix

ζ_i = zero-mean, unit-variance Gaussian random vector

η = tissue viscosity

λ = molecular mean free path of air

λ_{TB} = breathing period

μ = fluid viscosity

υ = kinematic viscosity of the air

ρ = fluid density

ρ_p = particle density

σ_{ij} = stress tensor

REFERENCES

[1] Nowak, N., Kakade, P. P., and Annapragada, A. V., 2003, "Computational Fluid Dynamics Simulation of Airflow and Aerosol Deposition in Human Lungs," Ann. Biomed. Eng., **31**, pp. 374-390.

[2] Tawhai, M. H., Pullan, A. J., and Hunter, P. J., 2000, "Generation of an Anatomically Based Three-Dimensional Model of the Conducting Airways," Ann. Biomed. Eng., **28**, pp. 793-802.

[3] Zhang, Z., and Kleinstreuer, C., 2002, "Transient Airflow Structures and Particle Transport in a Sequentially Branching Lung Airway Model," Phys. Fluids, **14**(2), pp. 862-880.

[4] Glezen, W. P., Loda, F. A., and Denny, F. W., 1982, "Parainfluenza Viruses," In: *Viral Infections of Humans* (2nd ed.), edited by Evans, A. S., Plenum Medical Book Company, New York, pp. 441-454.

[5] Chanock, R. M., Kim, H. W., Brandt, C. D., and Parrott, R. H., 1982, "Respiratory Syncytial Virus," In: *Viral Infections of Humans*, edited by Evans, A. S., Plenum Medical Book Company, New York, pp. 471-489.

[6] Bennett, W. D., Brown, J. S., Zeman, K. L., Hu, S.-C., Scheuch, G., and Sommerer, K., 2002, "Targeting Delivery of Aerosols to Different Lung Regions," J. Aerosol Med., **15**(2), pp. 179-188.

[7] Edwards, D. A., and Dunbar, C., 2002, "Bioengineering of Therapeutic Aerosols," Annu. Rev. Biomed. Eng., **4**, pp. 93-107.

[8] Kleinerman, J., 1974, "Industrial Pulmonary Diseases: Silicosis, Asbestosis, and Talc Pneumoconiosis," In: *Textbook of Pulmonary Diseases* (2nd ed.), edited by Baum, G. L., Little, Brown and Company, Boston, pp. 489-507.

[9] Kleinerman, J., 1974, "Industrial Pulmonary Diseases: Coalworker's Pneumonconiosis, Berylliosis, and Miscellaneous Causes," In: *Textbook of Pulmonary Diseases* (2nd ed.), edited by Baum, G. L., Little, Brown and Company, Boston, pp. 509-524.

[10] Tsuda, A., Butler, J. P., and Fredberg, J. J., 1994, "Effects of Alveolated Duct Structure on Aerosol Kinetics I. Diffusional Deposition in the Absence of Gravity," J. Appl. Physiol., **76**(6), pp. 2497-2509.

[11] Darquenne, C., 2001, "A Realistic Two-Dimensional Model of Aerosol Transport and Deposition in the Alveolar Zone of the Human Lung," J. Aerosol Sci., **32**, pp. 1161-1174.

[12] Henry, F. S., Butler, J. P., and Tsuda, A., 2002, "Kinematically Irreversible Acinar Flow: A Departure from Classical Dispersive Aerosol Transport Theories," J. Appl. Physiol., **92**, pp. 835-845.

[13] Haber, S., Yitzhak, D., and Tsuda, A., 2003, "Gravitational Deposition in a Rhythmically Expanding and Contracting Alveolus," J. Appl. Physiol., **95**, pp. 657-671.

[14] 1989, "Gray's Anatomy," In: *Gray's Anatomy* (37th ed.), edited by Williams, P. L., Churchill Livingstone, New York, pp. 1275, 1279.

[15] Prange, H. D., 2003, "Laplace's Law and the Alveolus: A Misconception of Anatomy and a Misapplication of Physics," Adv Physiol Educ, **27**(1), pp. 34-40.

[16] Haber, S., Butler, J. P., Brenner, H., Emanuel, I., and Tsuda, A., 2000, "Shear Flow over a Self-Similar Expanding Pulmonary Alveolus During Rhythmical Breathing," J. Fluid Mech., **405**, pp. 243-268.

[17] Darquenne, C., and Prisk, G. K., 2002, "Effect of Gravitational Sedimentation on Simulated Aerosol Dispersion in the Human Acinus," J. Aerosol Sci., **34**, pp. 405-418.

[18] Tsuda, A., Henry, F. S., and Butler, J. P., 1995, "Chaotic Mixing of Alveolated Duct Flow in Rhythmically Expanding Pulmonary Acinus," J. Appl. Physiol., **79**(3), pp. 1055-1063.

[19] ADINA R & D, 2003, *Automatic Dynamic Incremental Nonlinear Analysis Theory and Modeling Guide Volume I: Adina*. ADINA R & D, Watertown, MA, Pages, Chap.

[20] Drozdov, A. D., 1998, *Viscoelastic Structures: Mechanics of Growth and Aging*. Academic Press, San Diego, Pages, Chap.

[21] Karcher, H., Lammerding, J., Huang, H., Lee, R. T., Kamm, R. D., and Kaazempur-Mofrad, M. R., 2003, "A Three-Dimensional Viscoelastic Model for Cell Deformation with Experimental Verification," Biophys. J., **85**(5), pp. 3336-3349.

[22] 2004, "Cardiothoracic Imaging: Structure of the Bronchioles and Alveoli" [Online],Yale University School of Medicine, http://info.med.yale.edu/intmed/cardio/imaging/anatomy/bronchioles/index.html, Accessed: 2 June 2005.

[23] Weibel, E. R., 1986, "Functional Morphology of Lung Parenchyma," In: *Handbook of Physiology*, edited by Fishman, A., Macklem, P. T., Mead, J. and Geiger, S. R., American Physiological Society, Bethesda, Maryland, pp. 89-111.

[24] Levitzky, M. G., 1991, *Pulmonary Physiology*. McGraw-Hill, Inc., New York, Pages, Chap.

[25] Ochs, M., Nyengaard, J. R., Jung, A., Knudsen, L., Voig, M., Wahlers, T., Richter, J., and Gundersen, H. J. G., 2003, "The Number of Alveoli in the Human Lung," Am Jour Respir Crit Care Med, **169**, pp. 120-124.

[26] Haefeli-Bleuer, B., and Weibel, E. R., 1988, "Morphometry of the Human Pulmonary Acinus," Anat. Rec., **220**, pp. 401-414.

[27] Hills, B. A., 1999, "An Alternative View of the Role of Surfactant and the Alveolar Model," J. Appl. Physiol., **87**(5), pp. 1567-1583.

[28] Brudin, L. H., Rhodes, C. G., Valind, S. O., Wollmer, P., and Hughes, J. M. B., 1987, "Regional Lung Density and Blood Volume in Nonsmoking and Smoking Subjects Measured by Pet," J. Appl. Physiol., **63**(4), pp. 1324-1334.

[29] Hoppin, F. G., Stothert, J. C., Greaves, I. A., Lai, Y.-L., and Hildebrandt, J., 1986, "Lung Recoil: Elastic and Rheological Properties," In: *Handbook of Physiology*, edited by Fishman, A., Macklem, P. T., Mead, J. and Geiger, S. R., American Physiological Society, Bethesda, Maryland, pp. 195-215.

[30] The MathWorks. "Matlab" (7-R14 ed.). Natick, MA: The MathWorks, 2004.

[31] FLUENT, 2003, "Equations of Motion for Particles," In: *Fluent 6.1 User's Guide, Section 21.2.1*, Fluent Inc, Lebanon, New Hampshire.

[32] Li, A., and Ahmadi, G., 1992, "Dispersion and Deposiiton of Spherical Particles from Point Sources in a Turbulent Channel Flow," Aerosol. Sci. Technol., **16**, pp. 209-226.

[33] Einstein A, 1926, *Investigations on the Theory of the Brownian Movement*. E. P. Dutton and Co., New York, Pages, Chap.

[34] Abuzeid, S., Busnaina, A. A., and Ahmadi, G., 1991, "Wall Deposition of Aerosol Particles in a Turbulent Channel Flow," J. Aerosol Sci., **22**(1), pp. 43-62.

[35] Ghadiali, S. N., and Gaver, D. P., III, 2000, "An Investigation of Pulmonary Surfactant Physicochemical Behavior under Airway Reopening Conditions," J. Appl. Physiol., **88**(2), pp. 493-506.

APPENDIX A: Viscoelastic Tissue Modeling in ADINA

This model uses a spring in series with a Kelvin unit (a spring and a dashpot in parallel). Figure B1 shows the equivalent circuit where E_1 and E_2 are elastic moduli and η is the viscosity.

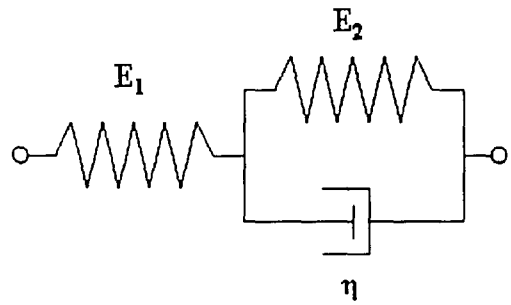

Fig. B1 Equivalent circuit for the standard viscoelastic material model.

The transient stress-strain solution for this system yields two new material properties—the shear and bulk moduli. These moduli depend on the elastic modulus, E(t), and the Poisson's ratio, υ, as shown in Eq. (A.1a) and (A.1b).

$$\text{(a)}\ G(t)=\frac{E(t)}{2(1+\upsilon)} \qquad \text{(b)}\ K(t)=\frac{E(t)}{3(1-2\upsilon)} \tag{A.1}$$

The elastic modulus in Eq. (7) depends on E_1, E_2, and the stress relaxation time, β, as given in Eq. (8).

$$E(t)=\frac{E_1E_2}{E_1+E_2}+\frac{E_1^{\,2}}{E_1+E_2}exp(-\beta\cdot t) \tag{A.2}$$

$$\text{or}\ E(t)=E_\infty+E_A\,exp(-\beta\cdot t) \tag{A.3}$$

Where the decay coefficient is:

$$\beta=\frac{E_1+E_2}{\eta} \tag{A.4}$$

This study assumes that $E_1 = 25\ E_2$, $E_2 = 10{,}000$ dyn/cm^2, and $\upsilon = 0.49$. The viscosity, η, varies in the range given in Table I. In ADINA, the moduli take the following form, where the subscript ∞ indicates the long term modulus.

$$G_\infty=\frac{E_\infty}{2(1+\upsilon)},G_A=\frac{E_A}{2(1+\upsilon)}\ \text{and}\ K_\infty=\frac{E_\infty}{3(1-2\upsilon)},K_A=\frac{E_A}{3(1-2\upsilon)} \tag{A.5}$$

APPENDIX B: Grid Pictures

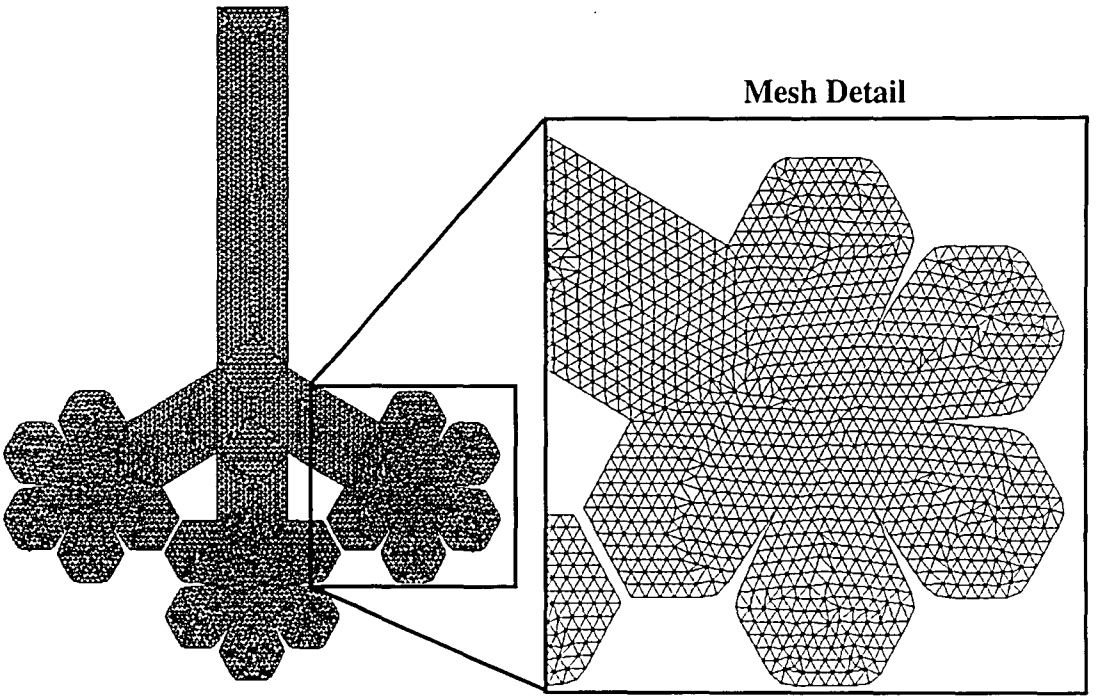

Fig. A1 Fluid domain mesh with alveolar sac detail. Element edge length is approximately 15 μm throughout the domain.

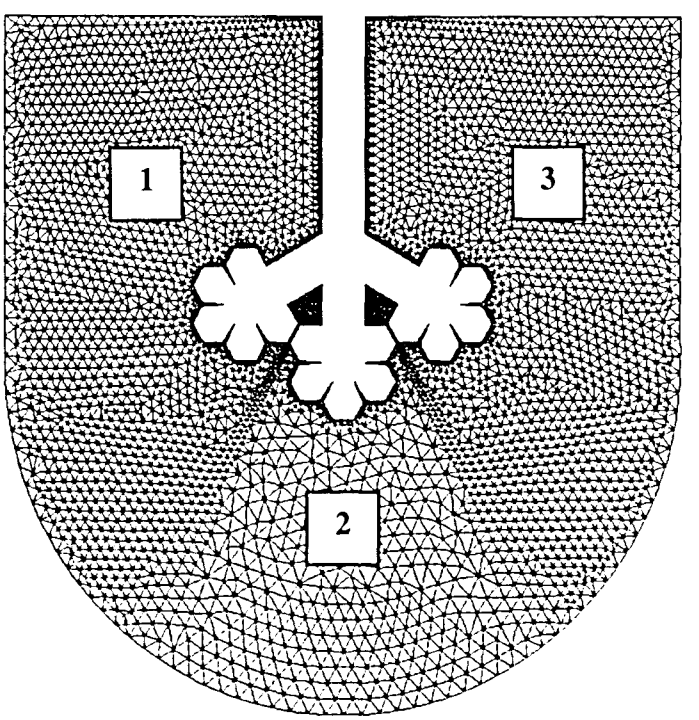

Fig. A2 Solid domain mesh. Node spacing is approximately 43 μm along the outer boundary. Mesh density differences between zones 1 and 3 and zone 2 are artifacts of the element growth algorithm; the boundary node spacing is the same.

APPENDIX C: Alveolar Expansion Ratio

To calculate the alveolar expansion ratio needed for physiologically-appropriate flow rates, start with the assumption that most of the change in lung volume during breathing occurs in the deformable alveoli. An average single alveolus at rest has a volume, $V_{alv} = 4.2 \times 10^6\ \mu m^3$, regardless of total lung size [25]. The average number of alveoli in adult human lungs, N_{alv}, is 480 million [25]. use this information to estimate V_{min}, the total alveolar lung volume when the lungs are at rest.

$$V_{\min} = V_{\text{alv, total}} = N_{alv} \times V_{alv} = 2016\ cm^3 \tag{C.1}$$

Adding the tidal breathing volume, V_{TB}, to the resting volume gives the maximum lung volume at the end of inspiration.

$$V_{\max} = V_{\min} + V_{TB} \tag{C.2}$$

define the specific volume excursion, C, to measure alveolar expansion [12]. If assume spherical alveoli for the purpose of volume calculation, can use the specific volume excursion to calculate the ratio of the maximum and minimum alveolar radii.

$$C = \frac{V_{\max} - V_{\min}}{V_{\min}} = \frac{V_{TB}}{V_{\min}} \tag{C.3}$$

$$C = \left(\frac{r_{\max}}{r_{\min}} \right)^3 - 1 \tag{C.4}$$

For a normal tidal breathing volume, V_{TB}=500 ml, the specific volume excursion C = 24.8%. The associated alveolar expansion ratio, (r_{max}/r_{min}) is approximately 8%.

APPENDIX D: Crank-Nicolson Integration Scheme

The Crank-Nicolson method integrates a differential equation of the form:

$$\frac{dx}{dt} + a(t)x = b(t) \tag{D.1}$$

in the following formulation

$$x_{n+1} = \left(1 + \frac{a_{n+1}\Delta t}{2}\right)^{-1}\left[\frac{\Delta t}{2}(b_{n+1} + b_n) + \left(1 - \frac{\Delta t}{2}a_n\right)x_n\right] \tag{D.2}$$

Where Δt is the integration time step and n is the current time step number. The Langevin equation (Eq. 8) can be recast in Crank-Nicolson form as follows.

$$\frac{dv_i^p}{dt} + F_D v_i^p = F_D v_i + \frac{g_i(\rho_p - \rho)}{\rho_p} + F_i^B = RHS \tag{D.3}$$

Where all quantities on the right hand side are either known or interpolated from the FSI flow field data. Thus, the Crank-Nicolson form of the Langevin equation reads:

$$\left(v_i^p\right)_{n+1} = \left(1 + \frac{F_D\Delta t}{2}\right)^{-1}\left[\frac{\Delta t}{2}(RHS_{n+1} + RHS_n) + \left(1 - \frac{F_D\Delta t}{2}\right)\left(v_i^p\right)_n\right] \tag{D.4}$$

Knowing the particle velocity from Eq. D.4 allows the solution of the position equation.

$$\frac{dx_i^p}{dt} = v_i^p \tag{D.5}$$

which can be solved in simplified Crank-Nicolson form for the new particle position.

$$\left(x_i^p\right)_{n+1} = \frac{\Delta t}{2}\left[\left(v_i^p\right)_{n+1} + \left(v_i^p\right)_n\right] + \left(x_i^p\right)_n \tag{D.6}$$

Vita

Hannah L. Dailey (nee Riger) was born in State College, Pennsylvania, on May 6, 1981. She was home-educated in Naples, Florida, by her parents, Charles and Susan Riger. As a high school student, she dual-enrolled at Edison Community College and then matriculated at Lehigh University in 1999. During her junior year, Hannah won the H.R. and Y.B. Wei award for Mechanical Engineering and Mechanics. After earning a Bachelor's Degree in Mechanical Engineering in 2002, she accepted a position with the Naval Surface Warfare Center in West Bethesda, Maryland. While at NSWC, she did computational fluid dynamics on submarines, surface ships, and propulsion systems. In 2003, Hannah returned to Lehigh for graduate school with her husband James. After a year of work with her advisor, Dr. Samir Ghadiali, she won a National Science Foundation Graduate Research Fellowship for computational modeling of fluid dynamics in the deep lungs.

Publications and Accepted Abstracts

- Ghadiali S.N., Dailey H.L., 2005, "Fluid-Structure Interactions and Microparticle Transport in Pulmonary Alveoli." In: *APS Division of Fluid Dynamics Annual Fall Meeting,* Podium Talk (Chicago, IL).

- Dailey H.L., Ghadiali S.N., 2005, "Brownian Diffusion and Fine Aerosol Dynamics in Pulmonary Alveoli." In: *Biomedical Engineering Society Annual Fall Meeting,* Poster Session (Baltimore, MD).

- Dailey H.L., Ghadiali S.N., 2005, "Fluid-Structure Analysis of Convective and Diffusive Particle Transport in Pulmonary Alveoli." In: *ASME Summer Bioengineering Conference,* Podium Talk (Vail, CO).

- Dailey H.L., Ghadiali S.N., 2004, "Computational Modeling of Particle Transport in Deformable Structures of the Deep Lung." In: *Biomedical Engineering Society Annual Fall Meeting,* Poster Session (Philadelphia, PA).

- Dailey H.L., Ebert M.P., Miller R.W., 2003, "Comparison of Structured and Unstructured RANS Computations for David Taylor Model Body 1." *Hydromechanics Directorate Report.* NSWCCD-50-TR-2003/039.

END OF TITLE